# Plastic deformation and fracture behavior of a Fe-modified Al3 Ti-base L12 intermetallic alloy

Hu, Gengxiang; Chen, Shipu; Wu, Xiaohua; Chen, Xiaofu



**Publisher's version / Version de l'éditeur:**
https://doi.org/10.1557/JMR.1991.0957
*Journal of Materials Research, 6, 5, pp. 957-963, 1991-05*

# Plastic deformation and fracture behavior of a Fe-modified $Al_3Ti$-base $L1_2$ intermetallic alloy

Hu Gengxiang, Chen Shipu, Wu Xiaohua, and Chen Xiaofu
*Department of Materials Science, Shanghai Jiao Tong University, Shanghai 200030, People's Republic of China*

(Received 1 October 1990; accepted 16 January 1991)

The microstructure of the ordered intermetallic alloy with a nominal composition of $Al_{66}Fe_9Ti_{24}$ is nearly single-phase $L1_2$ structure, with a few second phase agglomerates at some grain corners. Room temperature compression tests showed that this material exhibits a plastic strain of about 11% at fracture. Final fracture of the compression specimens occurred by a shear-off process along a surface oriented about 45 degrees to the compression axis. Fractographic analysis revealed that the fracture is transcrystalline and the fracture mode is mainly quasicleavage plus tearing. Transmission electron microscopy (TEM) was used to explore its deformation mechanisms. The dislocation density was low after homogenization, but is greatly increased during deformation. The deformation mode was found to be $\langle 110\rangle\{111\}$ slip instead of twinning as in $Al_3Ti$. The $a\langle 110\rangle$ superdislocations dissociated into two partials of $a/3\langle 211\rangle$-type, bounding a superlattice intrinsic stacking fault (SISF) on the $\{111\}$ slip plane.

## I. INTRODUCTION

The ordered intermetallic $Al_3Ti$ exhibits some attractive characteristics such as low density (3.4 g/cc) and high oxidation resistance, but is extremely brittle at room temperature. Since $Al_3Ti$ crystallizes into the tetragonal $DO_{22}$ structure, the major deformation mode was identified as $(111)[11\bar{2}]$ twinning, and slip occurred only at high temperatures.[1]

It is encouraging that the $DO_{22}$ $Al_3Ti$ can be changed to the cubic $L1_2$ ordered structure by replacing some amounts of Al with Cu, Ni, or Fe,[2–4] and also Mn and Cr, as has been reported recently.[5] Since the $L1_2$ structure is highly symmetrical and may have a sufficient number of slip systems for homogeneous deformation, it is expected that the ductility of modified $Al_3Ti$-base alloys will be greatly improved. This has attracted much attention and has led to a considerable amount of research in recent years. However, the results reported did not come up to the expectation. For instance, the $Al_3Ti$ alloys having $L1_2$ structure with Fe or Ni addition were also brittle and the fracture mode was still cleavage.[4,6] Therefore, further investigations aimed toward understanding the deformation behavior and the causes of low ductility of the $L1_2$-type $Al_3Ti$ alloy are necessary.

In this paper, an $L1_2$ intermetallic alloy with composition near $Al_{66}Fe_9Ti_{24}$ (at.%) was studied. This polycrystalline material shows appreciable compression ductility at room temperature. To understand the deformation behavior, a microstructural characterization of this ordered alloy was carried out and the deformation mode was studied by TEM analysis.

## II. EXPERIMENTAL

The $Al_3Ti$-based alloy with nominal composition $Al_{66}Fe_9Ti_{24}$ was prepared by arc-melting in argon with a nonconsumable tungsten electrode on a water-cooled copper hearth. The cast buttons were homogenized at 1373 K for 60 h to eliminate nonequilibrium segregation.

Compression specimens with dimensions $4 \times 4 \times 7$ mm were cut from the homogenized ingots. Tests were carried out in a Shimadzu DCS-25T machine. A crosshead speed of 0.05 mm/min was used, yielding a nominal strain rate of about 0.007/min. Some of the specimens were compressed only to a small amount of plastic strain (below 3%) for the purpose of exploring the deformation mechanisms.

Crystal structure determination and phase analysis were done by x-ray and electron diffraction methods. Microstructures and fractographic morphologies were examined using optical and scanning electron microscopy (OM and SEM). Chemical microanalysis was conducted with energy dispersive spectrometry (EDS) in the scanning electron microscope.

Thin foil specimens were prepared by twin jet polishing in a mixture of perchloric acid, butanol, and methanol (30:175:300 by volume) at 233 K and were examined by transmission electron microscopy (TEM) for the study of deformation substructure.

## III. RESULTS AND DISCUSSION

### A. Microstructures

Indexing of the x-ray diffraction patterns of the $Al_{66}Fe_9Ti_{24}$ alloy in either as-cast or homogenized con-

  

ditions indicated that all the resolvable peaks are identified with the fundamental and superlattice reflections of the ordered $L1_2$ structure, in contrast with the $DO_{22}$ of the unalloyed $Al_3Ti$ compound. Electron diffraction patterns obtained by TEM from the thin foils also verified the $L1_2$ structure.

The optical micrograph [Fig. 1(a)] of the as-cast alloy exhibits fine dendritic structure with second phase in the interdendritic regions. The dendritic structure was eliminated after 1373 K homogenization. However, the second phase could not be removed completely after such a treatment, agglomerates with irregular shapes occurring mainly at grain corners, as shown in Fig. 1(b).

As mentioned above, x-ray diffraction spectra did not reveal the existence of a second constituent in this alloy. This is due to their small quantities, which cannot produce detectable intensities of reflected x-rays.

The presence of an fcc $Al_2TiX$ phase has been verified in Al–Ti–X systems by several workers, where X = Fe,[7] Ni,[8] or Mn.[9] The second phase existing in the present alloy may also be of the $Al_2TiFe$-type, although the EDS microanalysis results performed in SEM did not fit with the equal amounts of Ti and Fe.

## B. Deformation behavior

### 1. Compressive plasticity

The results of compression tests at room temperature are summarized in Table I, and a typical load-deformation curve is shown in Fig. 2.

The plastic strains $\epsilon_f$ listed here were calculated from the crosshead displacement recorded by the testing machine after fracture. In fact, the crosshead displacement not only resulted from the elastic and plastic strains of the compressed specimen, but is also due to the closing of initial gaps and the deformation of the entire loading system. Therefore, a correction has been made to obtain the actual plastic strain at fracture, $\epsilon_p$, of the tested specimens, as shown in Table I. It can be seen that the $Al_{66}Fe_9Ti_{24}$ alloy exhibits an appreciable compressive ductility of about 11% at room temperature.

TABLE I. Compressive properties of the $Al_{66}Fe_9Ti_{24}$ alloy at room temperature (specimen: 4 × 4 × 7 mm).

| No. | Ultimate strength $\sigma_{max}$, MPa | Yield strength $\sigma_{0.2}$, MPa | Plastic strain, % | |
|---|---|---|---|---|
| | | | $\epsilon_f$ (recorded) | $\epsilon_p$ (corrected) |
| 1 | 486 | 286 | 14 | 10 |
| 2 | 405 | 272 | 12 | 9 |
| 3 | 510 | 258 | 15 | 12 |
| 4 | 481 | 240 | 16 | 13 |
| Average | 471 ± 45 | 264 ± 20 | 14 ± 2 | 11 ± 2 |

The strain distribution in the compressed specimen is inhomogeneous, which was observed with the naked eye by the flow markings in relief on the specimen surfaces. As the alloy is polycrystalline, these flow markings also indicate that slip propagated from one grain to the next throughout a region extending right across the specimen. To achieve such deformation, a minimum of five independent slip systems must be activated. Therefore, the good compression ductility of the $L1_2$-structured $Al_{66}Fe_9Ti_{24}$ alloy is attributed to a sufficient number of slip systems operating during deformation. Final fracture of the compression specimens occurred by a shear-off process along a surface oriented about 45 degrees to the compression axis. An example of the fractured specimens is shown in Fig. 3; an original specimen is also shown for comparison.

Fractographic analyses showed that the fracture is transcrystalline in nature and the fracture mode is

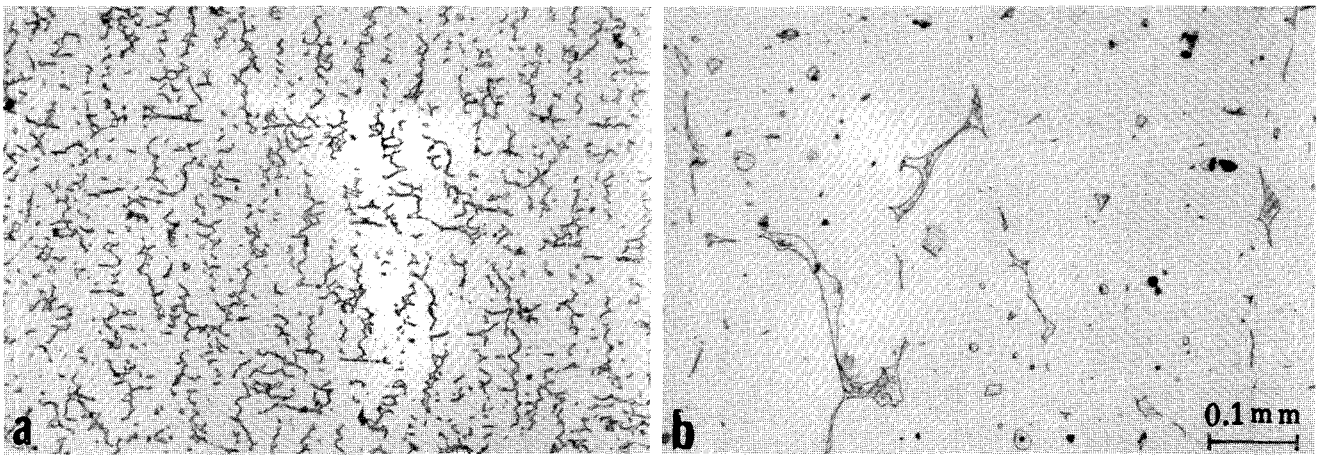


FIG. 1. Microstructures of the as-cast (a) and homogenized (b) $Al_{66}Fe_9Ti_{24}$ alloy.

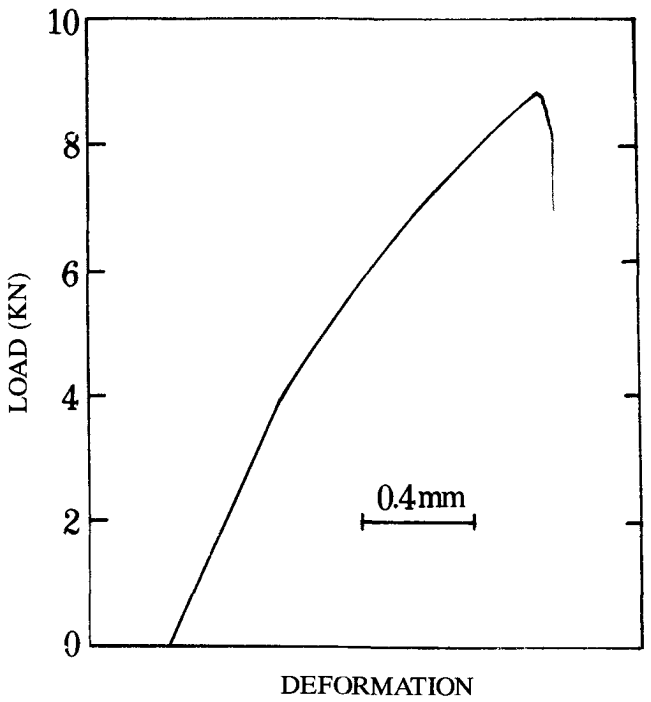


FIG. 2. Typical load-deformation curve of the $Al_{66}Fe_9Ti_{24}$ alloy tested under compression at room temperature.

mainly quasicleavage[10] plus tearing. An example of the fracture surface revealed by SEM is shown in Fig. 4(a), where the microscopic irregularities of quasicleavage surface and the linking tear ridges are apparent. A close examination at high magnification revealed that the quasicleavage regions are associated with dense steps of slip bands and curved subsurfaces [Fig. 4(b)]. These features together with the tear ridges observed in Fig. 4(a) illustrate that these regions were evidently deformed before fracture.

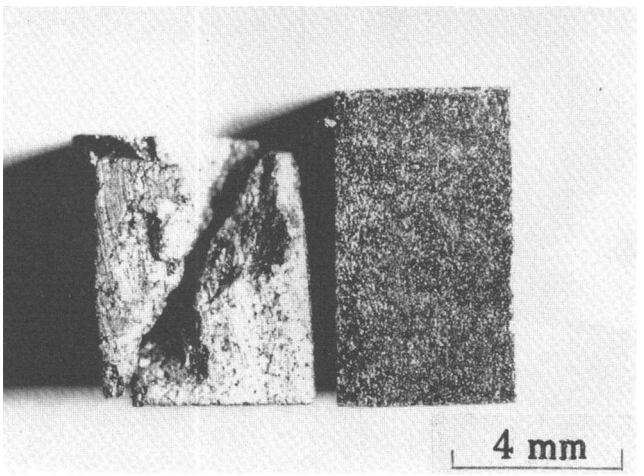


FIG. 3. Fractured (left) and original (right) specimens of the $Al_{66}Fe_9Ti_{24}$ alloy in compression tests.

## 2. Dislocation substructures

In order to explore the deformation mechanisms, dislocation configurations in the $L1_2$-structured $Al_{66}Fe_9Ti_{24}$ alloy compressed at room temperature have been analyzed by TEM. The general view is shown in Fig. 5. In contrast with the few straight free dislocations observed in the homogenized alloy (Fig. 6), the dislocation density is greatly increased after deformation. The moving dislocations introduced through deformation were locally pinned, as indicated by the bowing-out. They appeared to be in pairs, showing that the $\langle 101\rangle$ superdislocations dissociated into two partials, as confirmed by {220}-type reflections [Fig. 5(b)]. Using the weak beam technique, neither of the two partials was revealed to be further dissociated. No evidence of twinning was found. These results confirmed that dislocation slip must be the main mode of deformation of the present alloy, instead of twinning, as in the $DO_{22}$-type $Al_3Ti$ which has been shown to be extremely brittle at room temperature.

It is known that three kinds of planar faults occur on {111} planes of the $L1_2$ structure: antiphase boundary (APB), geometrical stacking fault (GSF, also called superlattice intrinsic stacking fault, SISF), and complex stacking fault (CSF), with displacement vectors $1/2\langle 110\rangle$, $1/3\langle 112\rangle$, and $1/6\langle 112\rangle$, respectively. The possible dissociation of an $a[\bar{1}01]$ superdislocation in the $L1_2$ structure is assumed to be any of three schemes—for instance, in the (111) plane:

1. $[\bar{1}01] \longrightarrow 1/6[\bar{1}\bar{1}2] + \text{CSF} + 1/6[\bar{2}11] + \text{APB}$
   $+ 1/6[\bar{1}\bar{1}2] + \text{CSF} + 1/6[\bar{2}11]$
2. $[\bar{1}01] \longrightarrow 1/2[\bar{1}01] + \text{APB} + 1/2[\bar{1}01]$
3. $[\bar{1}01] \longrightarrow 1/3[\bar{2}11] + \text{SISF} + 1/3[\bar{1}\bar{1}2]$

They have already been observed in different $L1_2$ alloys.[11–16]

In this study, superdislocation splitting into two partials labeled 1 and 2 in Fig. 5(b) was chosen to identify the configuration of dislocation dissociations and the nature of the planar fault bounded by such partials in detail.

Figure 7 is the TEM micrographs taken from the same particularly interesting region labeled in Fig. 5(b), but at higher magnification. Trace analysis indicated that the extended superdislocation is lying in the $(1\bar{1}1)$ plane and the labeled partials bounding the fault are parallel to the $[\bar{1}01]$ direction. Figure 7(a) shows a near (110) projection of the dislocation structure in which the fault plane seems to be perpendicular to $[1\bar{1}1]$. The partials 1 and 2 are along the trace $[\bar{1}01]$, the intersection of $(1\bar{1}1)$ and (111) planes, of which the latter is the projective plane of Fig. 7(b). These observations suggest that the dissociated superdislocation may have a total Burgers vector of $a[\bar{1}01]$ (or $a[10\bar{1}]$).

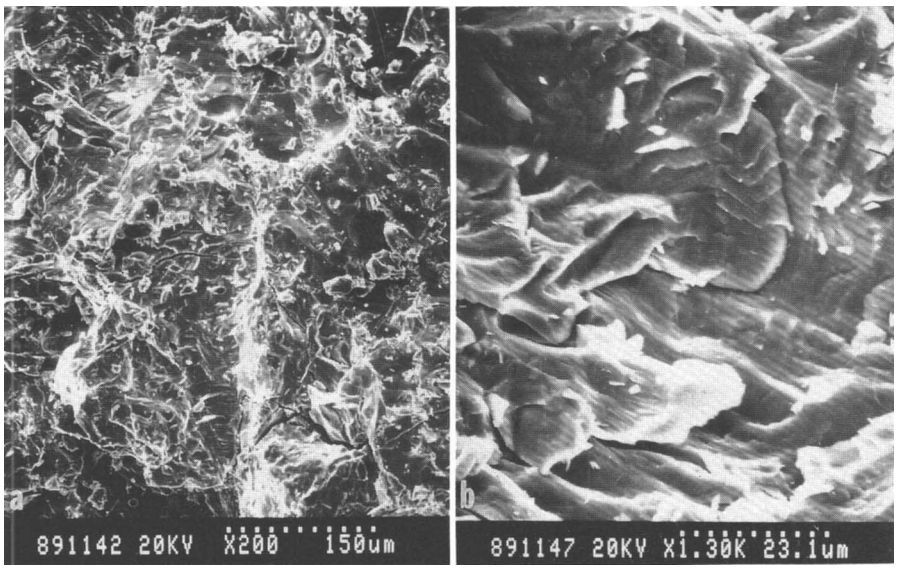


FIG. 4. SEM fractographs of the fracture surface of the $Al_{66}Fe_9Ti_{24}$ alloy.

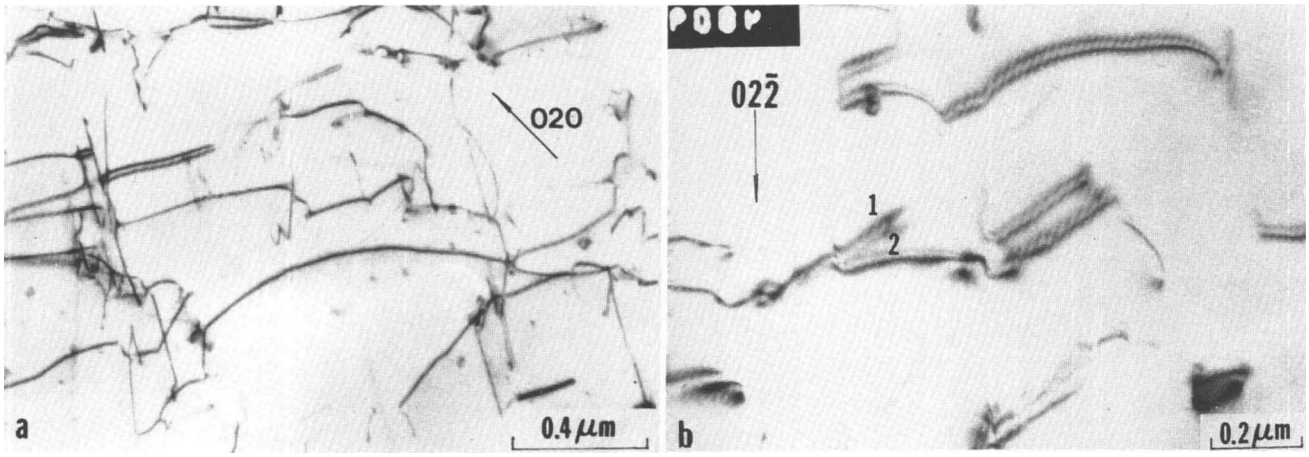


FIG. 5. Dislocation structures of the $L1_2$-structured $Al_{66}Fe_9Ti_{24}$ alloy deformed under compression at room temperature. (a) $\sigma$ = 418 MPa, $\epsilon$ = 2.83%; (b) $\sigma$ = 270 MPa, $\epsilon$ = 1.52%.

Contrast analysis of the partial dislocations has been carried out by using different reflections. The invisibility criteria for partial dislocations are $g \cdot b = 0$, $\pm 1/3$.[17] It has also been shown that for $s > 0$, a partial is in contrast when $g \cdot b = +2/3$, but out of contrast when $g \cdot b = -2/3$.[18] In the case of $g \cdot b = \pm 4/3$, a partial becomes invisible as $g \cdot b$ is positive and the reverse is true when it is negative.[19] Figures 5(b) and 7(a)–7(f) are some selected TEM micrographs, all of which were taken with the deviation parameter $s > 0$.

The fact that both partials 1 and 2 are not simultaneously in contrast or out of contrast for all these reflections used for Fig. 7 (sometimes one shows only weak residual contrast) confirmed that they must be of $1/3\langle 112\rangle$-type, and the dissociation of superdislocation $a[\bar{1}01]$ would occur in the form of scheme 3. Table II lists the $g \cdot b$ values of the partials dissociated from an $a[\bar{1}01]$ superdislocation in the $(1\bar{1}1)$ plane, together with

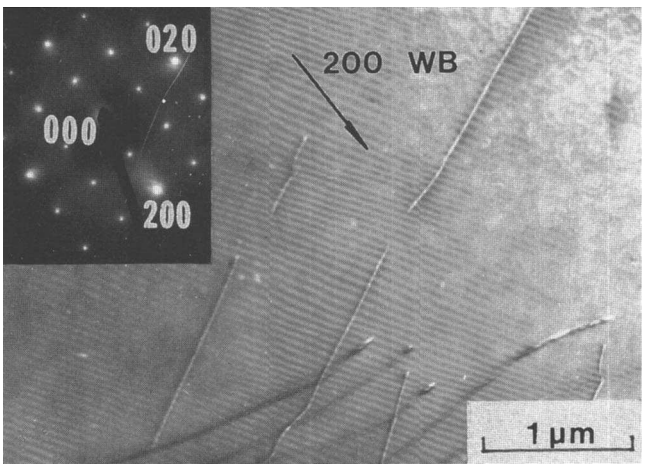


FIG. 6. Weak beam TEM micrograph shows straight free $a\langle 101\rangle$ dislocations in the undeformed $Al_{66}Fe_9Ti_{24}$ alloy after homogenization.

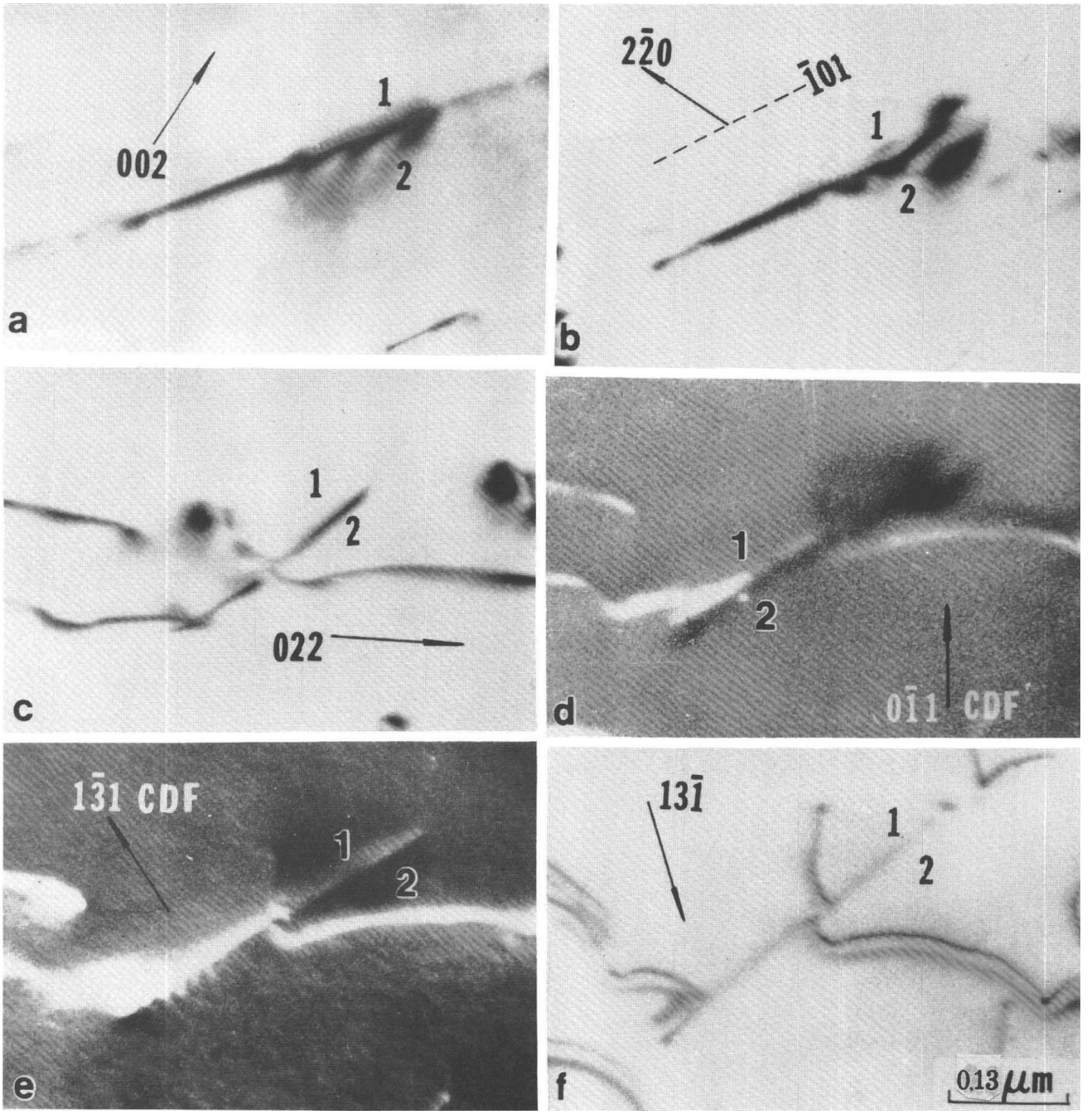


FIG. 7. TEM micrographs of the partials labeled 1 and 2 [the same as in Fig. 5(b)] for contrast analysis. See text and Table II.

the observed results. It can now be concluded that the Burgers vector is $a/3[\bar{2}\bar{1}1]$ for partial 1 and $a/3[\bar{1}12]$ for partial 2.

The intrinsic/extrinsic nature of the fault bounded by partials 1 and 2 has been determined using {111}-type reflections. Figure 8 was taken at a near (211) projection with $s = 0$, in which the fault plane $(1\bar{1}1)$ is inclined to the surface of the foil. For a stacking fault on the $(1\bar{1}1)$ plane, the displacement vector $\mathbf{R}_f$ is $\pm a/3[1\bar{1}1]$. In the BF image with $(1\bar{1}\bar{1})$ reflection, Fig. 8(a), both fringes at the intersections between the fault plane and the foil surfaces show dark contrast. When a CDF image with $(\bar{1}11)$ reflection, Fig. 8(b), is observed, the first fringe in the left (top) is found to be bright and the contrast of the right-side (bottom) fringe remains dark.

A simple way to identify the nature of a stacking fault was proposed by Gevers *et al.*[20] with a dark-field image only. For $g = \bar{1}11$, which belongs to the so-called type B reflection, when placing the origin of the diffraction vector at the center of the fault, it has been

TABLE II. Values of $g \cdot b$ for the possible Burgers vectors of the partials labeled 1 and 2 and the experimental observations of their visibilities.

| | Partial 1 ($b = 1/3[2\bar{1}1]$) | | Partial 2 ($b = 1/3[\bar{1}12]$) | | |
|---|---|---|---|---|---|
| $g$ | Expt. obser. | $g \cdot b$ | Expt. obser. | $g \cdot b$ | Fig. |
| 002 | V | +2/3 | I.V. | +4/3 | 7(a) |
| $2\bar{2}0$ | R.C. | −2/3 | V | −4/3 | 7(b) |
| 022 | I.V. | 0 | V | +2 | 7(c) |
| $0\bar{1}1$ | V | +2/3 | I.V. | +1/3 | 7(d) |
| $1\bar{3}1$ | V | +2/3 | I.V. | −2/3 | 7(e) |
| $13\bar{1}$ | V | −2 | I.V. | 0 | 7(f) |

V: visible; I.V.: invisible; R.C.: residual contrast.

found that $g$ points away from the bright outer fringe, i.e., toward the dark fringe at the right side in Fig. 8(b). This is the contrast feature expected from an intrinsic stacking fault.

The above observations lead us to conclude that the glide superdislocation with Burgers vector $a[\bar{1}01]$ has dissociated into two superpartials of $a/3\langle 112\rangle$-type bounding a SISF in the $(1\bar{1}1)$ plane:

$$[\bar{1}01] \longrightarrow 1/3[2\bar{1}1] + \text{SISF} + 1/3[\bar{1}12]$$

that is, in the $Al_{66}Fe_9Ti_{24}$ alloy the dislocation dissociation takes place in the mode of scheme 3.

Furthermore, such an $a\langle 101\rangle$ dislocation slip mechanism can be clearly seen in Fig. 9, which shows a planar array of slipping $a[10\bar{1}]$ superdislocations in the (111) glide plane and each of them dissociated into two partials. Contrast analysis also delineated that the superpartials are of $a/3\langle 211\rangle$-type, bounding SISFs.

Figure 10 shows the elongated dislocation loops in the (111) plane multiplied from a subboundary. This microscopic feature resembles the TEM observations of Takeuchi *et al.*[21] in deformed $Ni_3Ga$ $L1_2$ crystals, from which they have suggested that the source dislocations are self-trapped by thermally activated locking of screw segments due to the Kear–Wilsdorf mechanism, and the anomalous temperature dependence of the strength can be ascribable to this hardening mechanism of (111) slip.

Different dissociation configurations of the superdislocation have a strong influence on the deformation of the $L1_2$ materials. It has been found[2] that the $Al_{22}Fe_3Ti_8$ alloy shows anomalous increase of yield stress both in the low temperature region with decreasing temperature and in the high temperature region with increasing temperature, which is similar to that in a group of $L1_2$ alloys such as $Co_3Ti$. There has been no appropriate mechanism proposed to explain such yield behavior. Liu *et al.*[16] pointed out that the superdislocation with SISF would be responsible for the anomalous increase of yield stress at low temperatures. Micro cross slip may also operate in such alloys. As evidence, the dipoles of the extended dislocations were observed in the present alloy, as shown in Fig. 5. Furthermore, it is noteworthy that more than one configuration of dislocation dissociation sometimes occurs in certain $L1_2$ structures. For instance, widely extended GSFs have been identified in deformed $Ni_3Ga$[22] and $Ni_3Al$[23] as a result of the interaction of moving superdislocations with other lattice defects. It is not possible to affirm that the dissociation of scheme 3 is the unique mode for the alloy investigated here. These factors might lead to

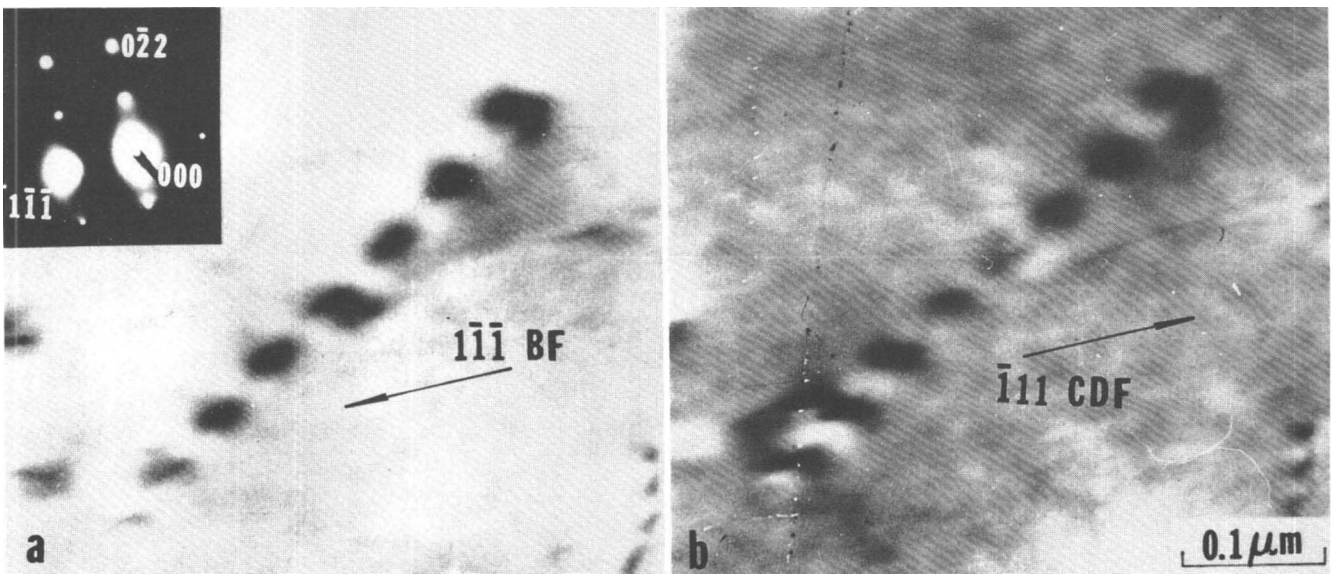


FIG. 8. Stacking fault bounded by the partials 1 and 2 as labeled in Figs. 5(b) and 7. See text for the details of analysis.

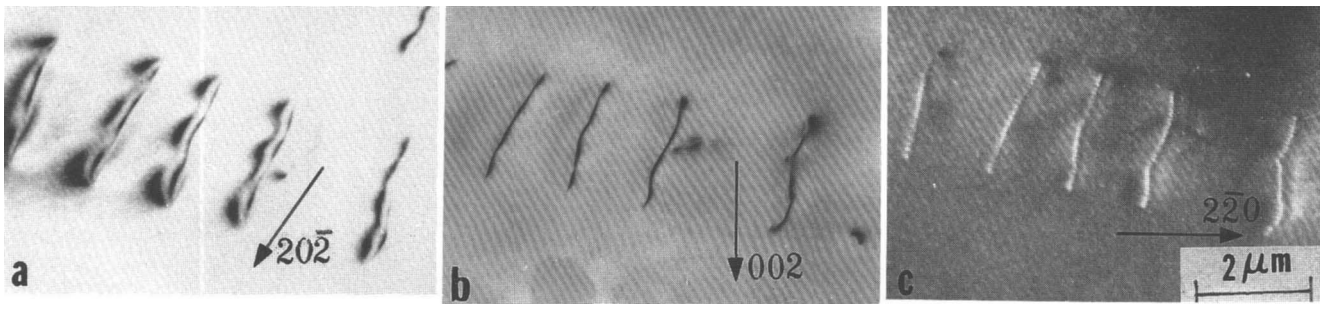


FIG. 9. A row of $a[10\bar{1}]$ superdislocation slipping in a (111) plane, dissociated into partials 1 and 2 of $a/3\langle 112\rangle$-type bounding SISFs.

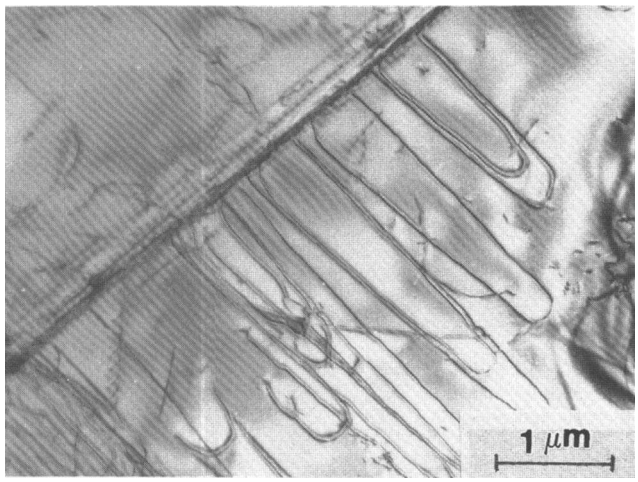


FIG. 10. The elongated dislocation loops in (111) plane multiplied from a subboundary.

an explanation for the anomalous dependence of yield stress over the entire temperature range.

## IV. CONCLUSIONS

(1) The $Al_3Ti$-base intermetallic alloy with a composition near $Al_{66}Fe_9Ti_{24}$ crystallizes into the $L1_2$ ordered structure. The second phase presented is possibly of $Al_2TiFe$-type.

(2) The $Al_3Ti$-base alloy containing Fe exhibits appreciable compressive ductility at room temperature.

(3) The alloy investigated deforms by a slip process at room temperature. TEM study on the substructure of the deformed specimens indicated that the $a[\bar{1}01]$ superdislocation dissociated into two superpartials bounding a SISF in the $(1\bar{1}1)$ glide plane, i.e.,

$$[\bar{1}01] \longrightarrow 1/3[\bar{2}\bar{1}1] + \text{SISF} + 1/3[\bar{1}12].$$

## REFERENCES

[1]M. Yamaguchi, Y. Umakoshi, and T. Yamane, in *High-Temperature Ordered Intermetallic Alloys, II,* edited by N. S. Stoloff, C. C. Koch, C. T. Liu, and O. Izumi (Mater. Res. Soc. Symp. Proc. **81**, Pittsburgh, PA, 1987), p. 275.
[2]K. S. Kumar and J. R. Pickens, Scripta Metall. **22**, 1015 (1988).
[3]J. Tarnacki and Y. W. Kim, Scripta Metall. **22**, 329 (1988).
[4]C. D. Turner, W. O. Powers, and J. A. Wert, Acta Metall. **23**, 2635 (1989).
[5]S. Zhang, J. P. Nic, and D. E. Mikkola, Scripta Metall. **24**, 57 (1990).
[6]E. P. George, W. D. Porter, H. M. Henson, W. C. Oliver, and B. F. Oliver, J. Mater. Res. **4**, 78 (1989).
[7]A. Seibold, Z. Metallk. **72**, 712 (1981).
[8]S. C. Huang, E. L. Hall, and M. F. X. Gigliotti, J. Mater. Res. **3**, 1 (1988).
[9]H. Mabuchi, K. Hirokawa, and Y. Nakayama, Scripta Metall. **23**, 1761 (1989).
[10]*Metals Handbook,* 9th ed. (ASM INTERNATIONAL, 1987), Vol. 12, p. 20.
[11]S. M. L. Sastry and B. Ramaswami, Philos. Mag. **33**, 375 (1976).
[12]A. Korner and H. P. Karnthaler, Philos. Mag. A **52**, 29 (1985).
[13]K. Suzuki, M. Ichihara, and S. Takeuchi, Acta Metall. **27**, 193 (1979).
[14]R. J. Taunt and B. Ralph, Philos. Mag. **30**, 1379 (1974).
[15]L. M. Howe, M. Rainville, and E. M. Schulson, J. Nucl. Mater. **50**, 139 (1974).
[16]Y. Liu, T. Takasugi, O. Izumi, and T. Takahashi, Acta Metall. **36**, 2959 (1988).
[17]A. Howe and M. J. Whelan, Proc. Roy. Soc. **A267**, 206 (1962).
[18]J. M. Silcock and W. J. Tunstall, Philos. Mag. **10**, 361 (1962).
[19]J. M. Oblak and B. H. Kear, in *Electron Microscopy of Materials,* edited by G. Thomas, R. M. Fulrath, and R. M. Fisher (University of California Press, 1972), p. 566.
[20]R. Gevers, A. Art, and S. Amelinckx, Physica Status Solidi **3**, 1563 (1963).
[21]S. Takeuchi, K. Suzuki, and M. Ichihara, Trans. JTM **20**, 264 (1979).
[22]H-r. Pak, T. Saburi, and S. Nenno, Scripta Metall. **10**, 1081 (1976).
[23]I. Baker and E. M. Schulson, Physica Status Solidi **A85**, 481 (1984).